JOURNAL OF GEOPHYSICAL RESEARCH, VOL. 104, NO. B8, PAGES 17,955–17,973, AUGUST 10, 1999

P wave anisotropy, stress, and crack distribution at Coso geothermal field, California

Jonathan M. Lees and Huatao Wu

Department of Geology and Geophysics, Yale University, New Haven, Connecticut

Abstract. A new inversion method for P wave anisotropy [*Wu and Lees*, 1999a] has been applied to high-precision, microseismic traveltime data collected at Coso geothermal region, California. Direction-dependent P wave velocity and thus its perturbation, are represented by a symmetric positive definite matrix A instead of a scalar. The resulting anisotropy distribution is used to estimate variations in crack density, stress distribution and permeability within the producing geothermal field. A circular dome-like structure is observed at the southwestern part of the geothermal region southwest of Sugarloaf Mountain. Using a linear stress-bulk modulus relationship, deviatoric stress is estimated to be 3 – 6 MPa at geothermal production depths (1 – 2 km), assuming all the anisotropy is related to stress. The stress field is compressional NNE-SSW and dilational WNW-ESE, coinciding with a previous, independent study using earthquake focal mechanisms. Following a theory on flat, elliptic cracks, residual crack density estimated from P anisotropy is ~0.0078 assuming crack aspect ratios $\gg 1:60$ and is ~0.041 when crack aspect ratios are close to 1:60. Residual crack orientation distribution is related to velocity anisotropy. On the basis of anisotropic part of crack density distribution function, the anisotropic part of permeability distribution may be calculated by a statistical approach via simple parallel fluid flow along cracks.

1. Introduction

Coso geothermal area of eastern California (Figure 1) is located between the strike-slip San Andreas fault system to the west and the extensional Basin and Range province to the east [*Duffield and Bacon*, 1981; *Roquemore*, 1980]. The geothermal field is located primarily in granitic, Mesozoic bedrock that has been heavily intruded by rhyolitic intrusions over the past several million years. The Coso region is seismically active, compared with other regions in the Owens Valley, averaging more than 20 microearthquakes per day [*Malin*, 1994]. Nearly half of the events are associated with geothermal injection-production activity, and the rest result from regional tectonics [*Malin*, 1994]. There has been extensive geophysical research of the region, including heat flow [*Combs and Rostein*, 1976] and regional seismic attenuation [*Young and Ward*, 1980; *Walck and Clayton*, 1987; *Walck*, 1988]. Detailed P and S wave velocity models for the geothermal area were generated from microseismic traveltime data [*Wu and Lees*, 1999b].

Recent research on S wave anisotropy and crack distribution in the Coso region provided estimates of crack distribution based on shear wave splitting observed on selected earthquake records [*Luo and Rial*, 1997]. These anisotropy results, however, do not provide uniform coverage of the field, because of the limited number and geographic distribution of S wave splitting observations. To further delineate the fracture distribution in the geothermal field and to facilitate regional tectonic research and geothermal production, more detailed knowledge of anisotropic structures is required. We present here an application of a new method of anisotropic inversion applied to P wave travel times at Coso.

Seismic anisotropy is pervasive in the Earth's crust and upper mantle. The effects of anisotropy on seismic waves are generally not of second order, compared with isotropic inhomogeneities [*Anderson*, 1989; *Babuska and Cara*, 1991], and so should, in principle, be addressed in investigations of three-dimensional variations of seismic parameters. In geothermal fields, velocity anisotropy was previously observed and associated with fracture zones [*Leary and Henyey*, 1985; *Luo and Rial*, 1997]. Both internal rock fabric and external physical conditions give rise to velocity anisotropy. Possible origins include preferred crystal orientation, lithological layering, crack alignment, deviatoric stress field, and fluid flow [*Schön*, 1996]. A material containing an aligned system of cracks is effectively anisotropic for elastic waves, while materials containing randomly oriented microcracks exhibit bulk isotropy [*Hudson*, 1981, 1994; *Crampin*, 1984]. Application of a deviatoric stress can preferentially open and close cracks, however, depending on their orientation with respect to the principal

Paper number 1999JB900158.
0148-0227/99/1999JB900158$09.00

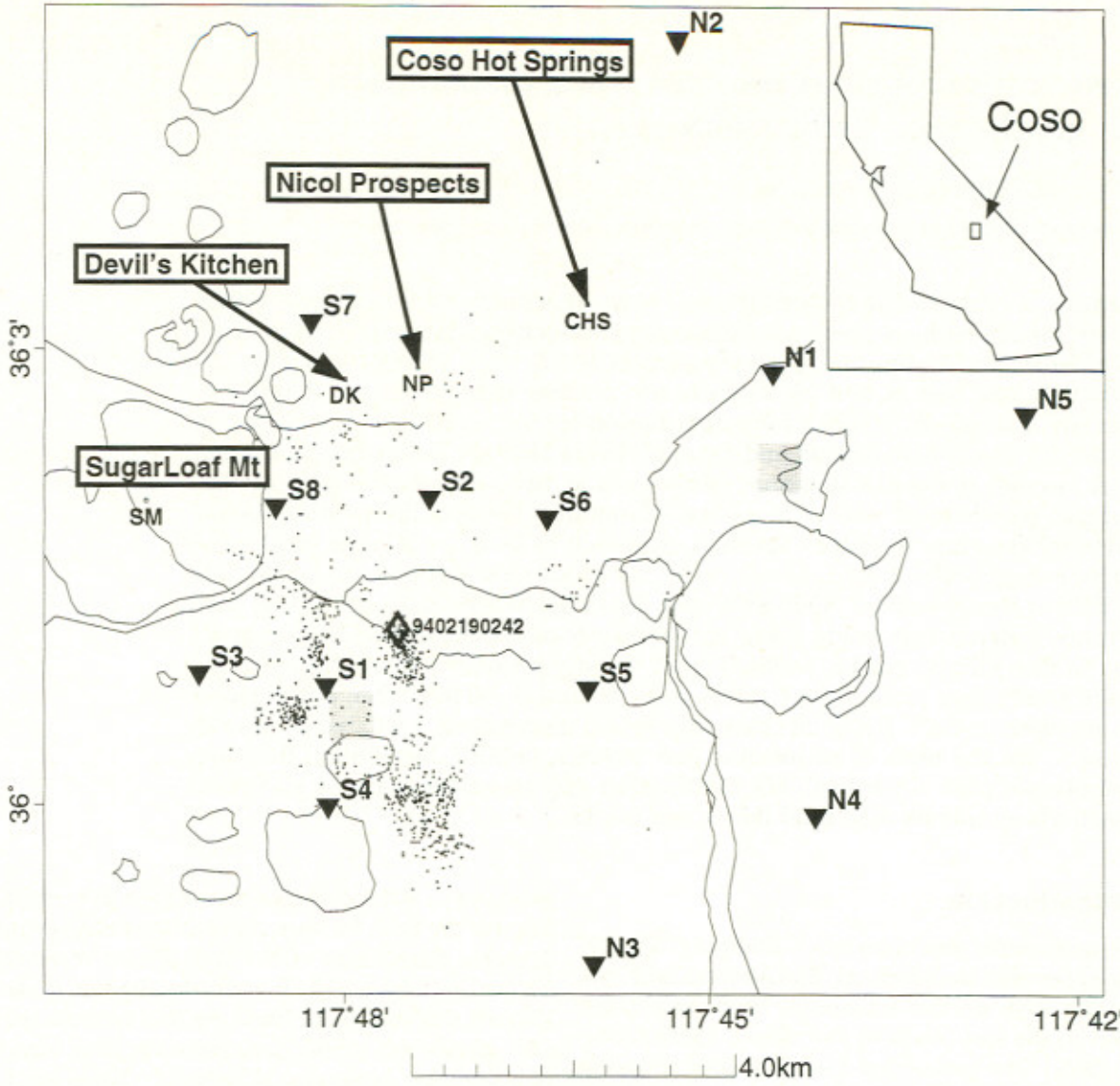

Figure 1. Map view of the geothermal field region at Coso, California. Inset shows location of Coso in California. Highlighted circular features are rhyolitic domes. Small dots represent seismic events used in this study, and triangles are seismic stations in Table 1 of *Wu and Lees* [1999b]. Important geographic locations are annotated: DK, Devil's Kitchen; NP, Nicol Prospects; CHS, Coso Hot Springs; and SM, Sugarloaf Mountain. The event shown in Figure 2 is plotted as a diamond. The two shaded areas are locations of blocks where ray coverage is illustrated in Figure 3.

stress direction [*Nur*, 1971]. The resultant, nonuniform crack orientation distribution can introduce elastic anisotropy into an otherwise isotropic material [*Nur and Simmons*, 1969]. Measurements of velocity anisotropy have been used to derive the density distribution of crack orientation, which can be used, in turn, to predict permeability anisotropy for fluid flow [*Gibson and Toksöz*, 1990]. Researchers modeling geothermal field evolution would like to have access to this information, which will ultimately provide constraints on forward modeling of fluid flow in the crust.

In most investigations of traveltime tomography in the shallow crust, velocity anisotropy is neglected. Synthetic tests show that in a large traveltime data set that includes rays distributed in all directions, anisotropic effects statistically cancel and isotropic inversions provide reasonable results [*Wu and Lees*, 1999b]. Ignoring effects of anisotropy, however, could potentially result in erroneous structures if ray directional coverage is not perfect, as is common in real tomographic cases [*Pratt et al.*, 1993]. To minimize potential biases associated with anisotropy where ray distributions are heterogeneous, velocity parameterization that takes anisotropic structure into account is required. One of the major hurdles for full anisotropic traveltime inversion is the lack of an efficient method to cope with the nonlinearity of traveltime formulations [*Hirahara*, 1988]. In this paper, we follow a recently developed linear parameterization of

anisotropic velocity [*Wu and Lees*, 1999a] and invert for P wave anisotropy at the Coso geothermal area. Differential, or deviatoric, stress fields and residual crack density are then estimated from the three-dimensional distribution of velocity anisotropy. The resultant crack density distribution provides further insight into the permeability distribution of the geothermal field, which, in turn, has potential uses for geothermal exploration and production.

2. Observational Evidence of Seismic Anisotropy at Coso

We expect to find seismic anisotropy in the Coso geothermal area, given observed extensive faulting, microcracking, and extreme heterogeneity. This expectation is confirmed by the presence of S wave birefringence previously observed here [*Shalev and Luo*, 1995; *Luo and Rial*, 1997]. Figure 2 shows S wave splitting at station S1 for an event on February 19, 1994. The bulk anisotropy along this particular ray path is estimated to be ~3.5% on the basis of ratio of S splitting time to S wave travel time (see Figure 1 for location of event). The azimuthal dependence of the apparent velocity, defined as the length of the ray path divided by the total travel time, with station corrections removed, can be modeled by fitting the data using an elliptical velocity function with azimuth (a linear combination of $\sin 2\theta$ and $\cos 2\theta$, where θ is the orientation angle of the fast direction). The bulk anisotropy of the apparent velocity is thus found to be 4.5%, with the slow direction at N25.2°E. This direction is parallel to one set of Coso faults (NNE-SSW) observed extensively throughout the field [*Roquemore*, 1980]. A previous S wave splitting study identified three predominant subsurface fracture directions [*Luo and Rial*, 1997]. Shear wave anisotropy from the S wave splitting was subsequently used to estimate three-dimensional crack density on the basis of simple models relating anisotropy to crack density. Models based on shear wave splitting, however, are severely limited by small data sets and limited geographic distribution of ray paths.

Although shear wave splitting indicates the existence of velocity anisotropy, absence of shear wave splitting does not indicate absence of seismic anisotropy. If anisotropy along a ray path is randomly oriented, we do not expect to observe significant S wave splitting. In this case, a more formal, systematic method to detect anisotropy is needed. In the present paper, we use P wave travel times, rather than S wave splitting, to invert for anisotropic structures. One advantage of using P wave travel times, as opposed to S-wave splitting, is

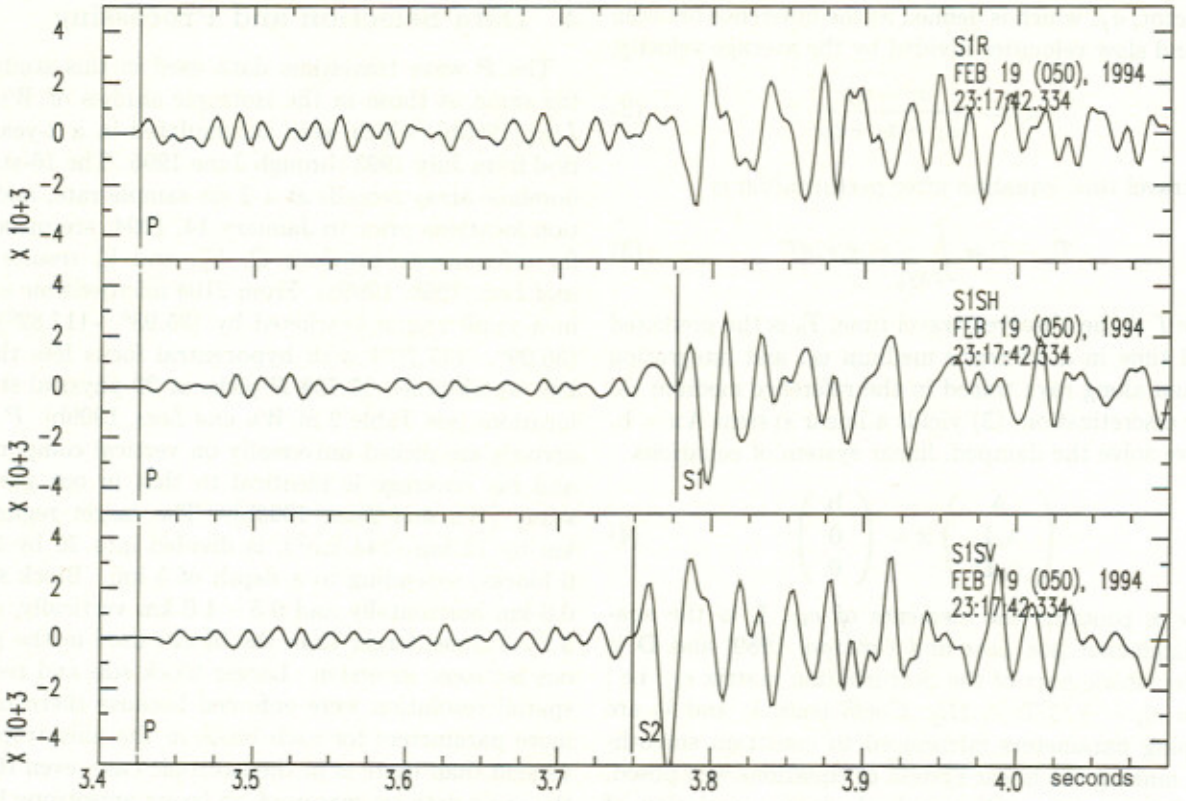

Figure 2. Observed S wave splitting: unfiltered velocity record of event 9402190242. The original record is rotated to radial, SV, and SH directions. The arrival time difference of the split S pulses is 0.028 s (28 ms). The total P wave travel time of this record is 0.460 s (460 ms) and the total S wave travel time is 0.806 s. The average anisotropy along the ray path is about 3.5 %.

that accurate P wave travel times are available in large quantities, allowing for simple formal inversion, in contrast to S wave splitting data, which are extremely labor intensive. For example, in the work of *Luo and Rial* [1997], 450 S splitting observations were used to determine Coso crack density, in an area 4 times larger than the present study. The ray path coverage of the S wave splitting study was poor and included data located far outside the seismic network, where hypocenter determinations are questionable at best. In the present study, we constrain our models with more than 17,000 P picks, a considerable improvement over previous studies.

3. Inversion Method

Anisotropy of P wave velocity v can be represented approximately by a symmetric, positive definite matrix A [*Wu and Lees*, 1999a],

$$v = A_{ij}\hat{r}_i\hat{r}_j \tag{1}$$

where $\hat{r}_i$ is a unit vector along the wave propagation direction. Using an isotropic reference velocity model v_0, we have $A_{ij} = v_0(I_{ij} + e_{ij})$, where e_{ij} is a small, anisotropic perturbation. The velocity surface represented by (1) is a squared ellipsoid whose three principal axes are the three eigenvectors of A, and the three principal velocities are eigenvalues a_i of matrix A. We estimate the presence of anisotropy by introducing an anisotropic factor, a_f, which is defined as the difference between fast and slow velocities divided by the average velocity,

$$a_f = 3\frac{a_1 - a_3}{a_1 + a_2 + a_3} \tag{2}$$

The travel time equation after perturbation is

$$T_0 - T \approx \int_{\text{ray}_0} e_{ij}\hat{r}_i\hat{r}_j dT \tag{3}$$

where T is the observed travel time, T_0 is the predicted travel time in a reference medium v_0, and integration is taken along rays traced in the reference medium v_0. After discretization, (3) yields a linear system $\mathbf{Ax} = \mathbf{b}$, and we solve the damped, linear system of equations

$$\begin{pmatrix} \mathbf{A} \\ \lambda_1\mathbf{L} \\ \lambda_2\mathbf{D} \end{pmatrix} \mathbf{x} = \begin{pmatrix} \mathbf{b} \\ \mathbf{0} \\ \mathbf{0} \end{pmatrix} \tag{4}$$

where $\mathbf{x}$ contains the elements of e_{ij}, $\mathbf{L}$ is the spatial Laplacian [see *Lees and Crosson*, 1989] and $\mathbf{D}$ is the deviatoric part of the perturbation matrix e_{ij}, i.e., $D_{ij} = e_{ij} - (1/3)\mathrm{Tr}(e_{ij})I_{ij}$. Coefficients λ_1 and λ_2 are damping parameters introduced to constrain smoothness, making the linear system of equations well posed. The linear system (4) is solved using a variation of LSQR constrained by the Laplacian regularization of *Lees and Crosson* [1989].

Several different strategies of regularization can be applied to (4), and in this study, we chose to damp isotropic and anisotropic parts separately via $\mathbf{L}$ and $\mathbf{D}$. Heterogeneous ray coverage, however, can introduce undesirable noise in anisotropic P wave inversions [*Wu and Lees*, 1999a]. If a block is penetrated by rays coming from a single direction, anisotropic information can not be retrieved from the data, and anisotropic inversion should generally be avoided. To cope with this difficulty and to force isotropy when ray coverage is inadequate, we include a separate damping parameter λ_2 to control the deviatoric part of e_{ij} in the inversion. When the ray coverage is deemed inadequate, the damping parameter forces the isotropic part, $\mathbf{D}$, to absorb the variability of the data for a particular block. The form of $\mathbf{D}$ in (4) for a single block is

$$\mathbf{De} = \begin{pmatrix} \frac{2}{3} & -\frac{1}{3} & -\frac{1}{3} & & & \\ -\frac{1}{3} & \frac{2}{3} & -\frac{1}{3} & & & \\ -\frac{1}{3} & -\frac{1}{3} & \frac{2}{3} & & & \\ & & & 1 & & \\ & & & & 1 & \\ & & & & & 1 \end{pmatrix} \begin{pmatrix} e_{11} \\ e_{22} \\ e_{33} \\ e_{12} \\ e_{13} \\ e_{23} \end{pmatrix} = \begin{pmatrix} 0 \\ 0 \\ 0 \\ 0 \\ 0 \\ 0 \end{pmatrix} \tag{5}$$

Linear inversion with an isotropic ray-tracing algorithm is used in this paper. We are currently developing an anisotropic ray-tracing method in matrix medium. With the introduction of ray tracing in anisotropic, matrix media, we will be able to compute rays and locate events using anisotropic models, leading to full, nonlinear solutions of (4).

4. Data Selection and Processing

The P wave traveltime data used in this study are the same as those in the isotropic studies of *Wu and Lees* [1999b], which were accumulated in a 2-year period from July 1993 through June 1995. The 16-station borehole array records at a 2 ms sample rate, and station locations prior to January 14, 1994, are presented for reference to previous Q, V_p, and V_s results [*Wu and Lees*, 1996, 1999b]. From 2104 microseismic events in a small region bracketed by (35.98°, -117.82°) and (36.09°, -117.70°) with hypocentral focus less than 6 km, we obtained 17,758 P picks at 29 physical station locations [see Table 2 in *Wu and Lees*, 1999b]. P wave arrivals are picked universally on vertical components, and ray coverage is identical to that in our previous study [*Wu and Lees*, 1999b]. The target region, 12 km by 12 km (144 km^2), is divided into 20 by 20 by 6 blocks, extending to a depth of 5 km. Block size is 0.6 km horizontally and 0.5 – 1.0 km vertically, about 3 by 3 times larger than the blocks used in the previous isotropic inversion. Larger block size and reduced spatial resolution were enforced because there are six more parameters for each block in the anisotropic inversion than there is in the isotropic case, even though the same data set was used, so larger anisotropy blocks provide similar constraints on block parameters. gv We start with a one-dimensional, isotropic reference velocity model derived for standard earthquake locations in the geothermal field [*Wu and Lees*, 1999b; E. Shalev, personal communication, 1996]. Hypocenters

and ray tracing relative to the one-dimensional (1-D) model were used to predict travel times of each ray in each block penetrated, where differences between predicted and measured travel times, $T_0 - T$, are the data. We are confident that for most parts of the model, especially near station S1, anisotropy is well constrained. While in the central part of the target, directional ray coverage is fairly complete, near the edge of the model, coverage is poor (Figure 3), and we are considerably less confident about the resulting models. To compensate for the lack of information in the boundary blocks, anisotropy is controlled and virtually eliminated by adjusting regularization parameter λ_2. Picking errors in the data range from 6 to 15 ms; these errors are small compared with total travel times. Average relative picking errors are $< 1.5\%$, taken to be the noise level of the data set.

Root-mean-square residual deviation of data before inversion is 19.3 ms reduced to ~15.5 ms after inversion. The remnant residuals are much larger than the noise level of the data set. Variance reduction of the inversion is thus 36.0%, slightly less than the previous isotropic inversion. Considering that many fewer blocks (2400 compared with 32,400) are used in this study, the variance reduction achieved is comparable to previous, purely isotropic analyses.

The isotropic part of the new inversion results, $\mathrm{Tr}(e_{ij})$, is similar to results obtained by *Wu and Lees* [1999b]. For example, high velocities are observed at depths 1–2 km below Coso Hot Springs (CHS) in both inversions, and high velocities are seen between stations S2 and S6. However, we normally expect to see some differences due to the trade-off between anisotropy and isotropy for any specific, imperfect ray coverage [*Pratt et al.*, 1993; *Wu and Lees*, 1999a]. These differences are discussed in some detail, from a purely theoretical point of view, by *Wu and Lees* [1999a]. Specifically, we see a moderately high velocity between S1 and S4 at depths 2–3 km, where low velocity was previously reported [*Wu and Lees*, 1999b]. In the current inversion the amplitude of the isotropic part is diminished relative to simple, undamped isotropic inversion because of additional regularization factors λ_1 and λ_2. Furthermore, part of the data variability is fit by anisotropic parameters, which reduces the overall size of isotropic perturbations. The parameters $\lambda_1 = 0.3$ and $\lambda_2 = 0.5$ were chosen for the final inversion, after determination by trial and error and considering trade-offs of model variability and spatial resolution. Damping in the anisotropic inversion is larger than that in the previous isotropic inversion [*Wu and Lees*, 1999b], primarily because anisotropic information contained in the data set is less constrained computationally, producing models that are more irregular, such that more damping is needed to yield smooth results. The average isotropic perturbation in the final models (Figure 4), taken over the whole target, is small (0.1%), and its depth profile is provided in Table 1. We note that the broadscale features correlate with previous, isotropic inversion [*Wu and Lees*, 1999b]. Isotropic velocity around S1-S3-S4 shows a low-velocity zone at shallow depths (< 2 km) and a high-velocity anomaly at depths > 2 km. Coso Hot Springs appears as high velocity, as in the isotropic inversion. Another prominent high-velocity feature is found east of station S6, close to the S2-S6 high-velocity zone found previously [*Wu and Lees*, 1999b].

5. Anisotropic Inversion Results

The average anisotropic factor $\bar{a}_f$ for the whole target is ~3.88%, and the layerwise profile of anisotropy is listed in Table 1. The largest anisotropy, $a_f = 5.2\%$, is found at depths of 1–2 km. In fact, the anisotropic factor varies slightly from 4.7 to 5.2% at depths of 0.5–3 km. Since the top and bottom layers are heavily damped, they show considerably less anisotropy.

The three-dimensional distribution of anisotropic factor a_f is shown in Figure 5, where blocks penetrated by

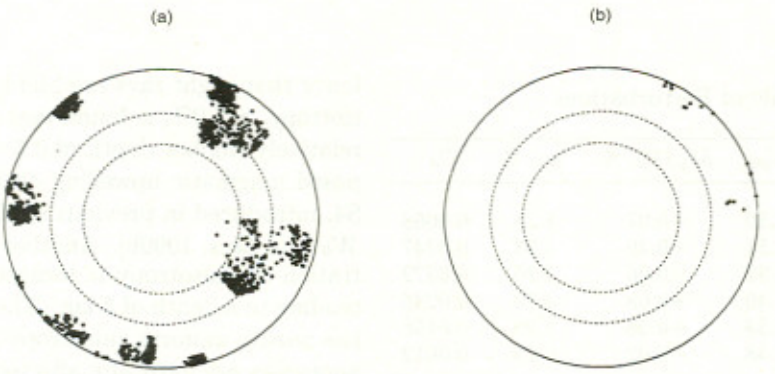

Figure 3. Typical block ray coverage in a critical region. The plots are equal area projections of rays through the block (lower hemisphere). Small shaded regions in Figure 1 show locations. (a) Block 904 (depth 1–2 km, layer 3). This block is located close to the center of the target (left block in Figure 1). There are 1773 rays passing through this block, providing good ray coverage. (b) Block 1414 (depth 2–3 km, layer 4). This block is located at the eastern part of the target between N1 and N5 (right block in Figure 1). There are 18 rays passing through this block, and ray coverage is poor.

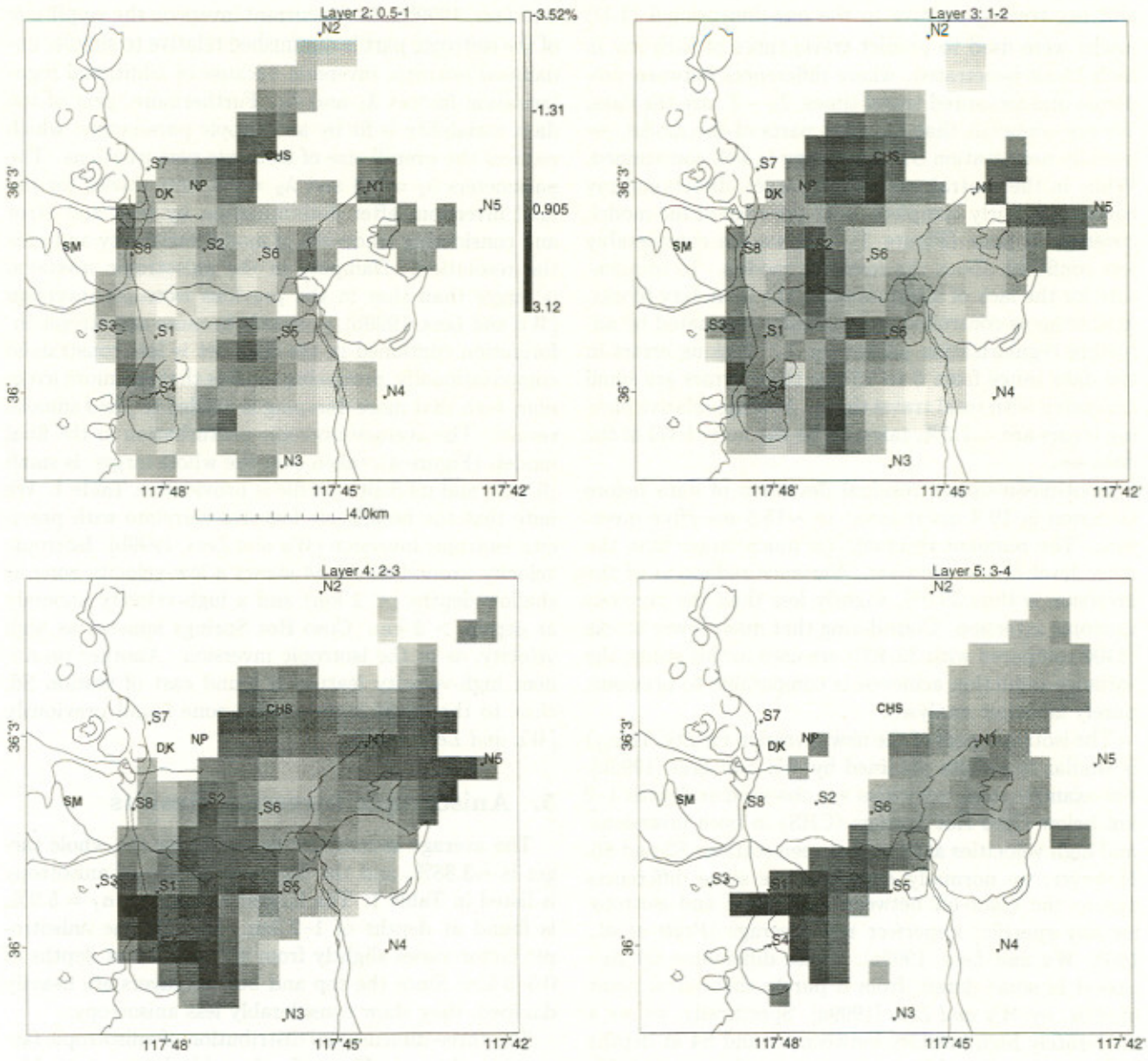

Figure 4. Isotropic part of perturbation e_{ij}. The gross anomalies are similar to previous results of *Wu and Lees* [1999b].

Table 1. Depth Profile of Perturbations

Layer	Depth, km	V_{p0}	$\delta V_p/V_p$, %	a_f, %	C_d
1	0.0–0.5	4.50	−0.07	1.31	0.0068
2	0.5–1.0	4.51	−0.40	4.73	0.0247
3	1.0–2.0	4.92	−0.06	5.20	0.0272
4	2.0–3.0	5.46	+0.68	4.72	0.0246
5	3.0–4.0	5.54	+0.38	2.99	0.0156
6	4.0–5.5	5.58	−0.02	0.23	0.0012

V_{p0} is isotropic P velocity; $\delta V_p/V_p$ is anisotropic perturbations; a_f is anisotropy factor; and C_d is residual crack density. Crack density estimates assume an aspect ratio of 1/38, i.e., $c = 1.915$. All values are layer averages, and values in the fourth and fifth columns are percentage figures, for example, $100^*\delta V_p/V_p$ for V_p perturbation.

fewer than eight rays are blanked out. The largest anisotropy, > 8.0%, is found east of stations S1-S4 at the relatively shallow depth of 0.5 – 1.0 km, close to a proposed magmatic upwelling center near stations S1-S3-S4, introduced in previous studies [*Wu and Lees*, 1996; *Wu and Lees*, 1999b]. Another spatially larger concentration of anisotropy is located around station S6 extending to a depth of 3 km. The remainder of the target has mostly uniform anisotropy of 1–2%, although these anomalies are naturally affected by smearing effects associated with heavy damping. Vertical cross sections (Figure 6, left) reveal a prominent anisotropic body between stations S1 and S4, with a horizontal dimension of ~1 km.

Horizontal and vertical planar projections of fast axes of velocity-squared ellipsoids are presented in Figures 7

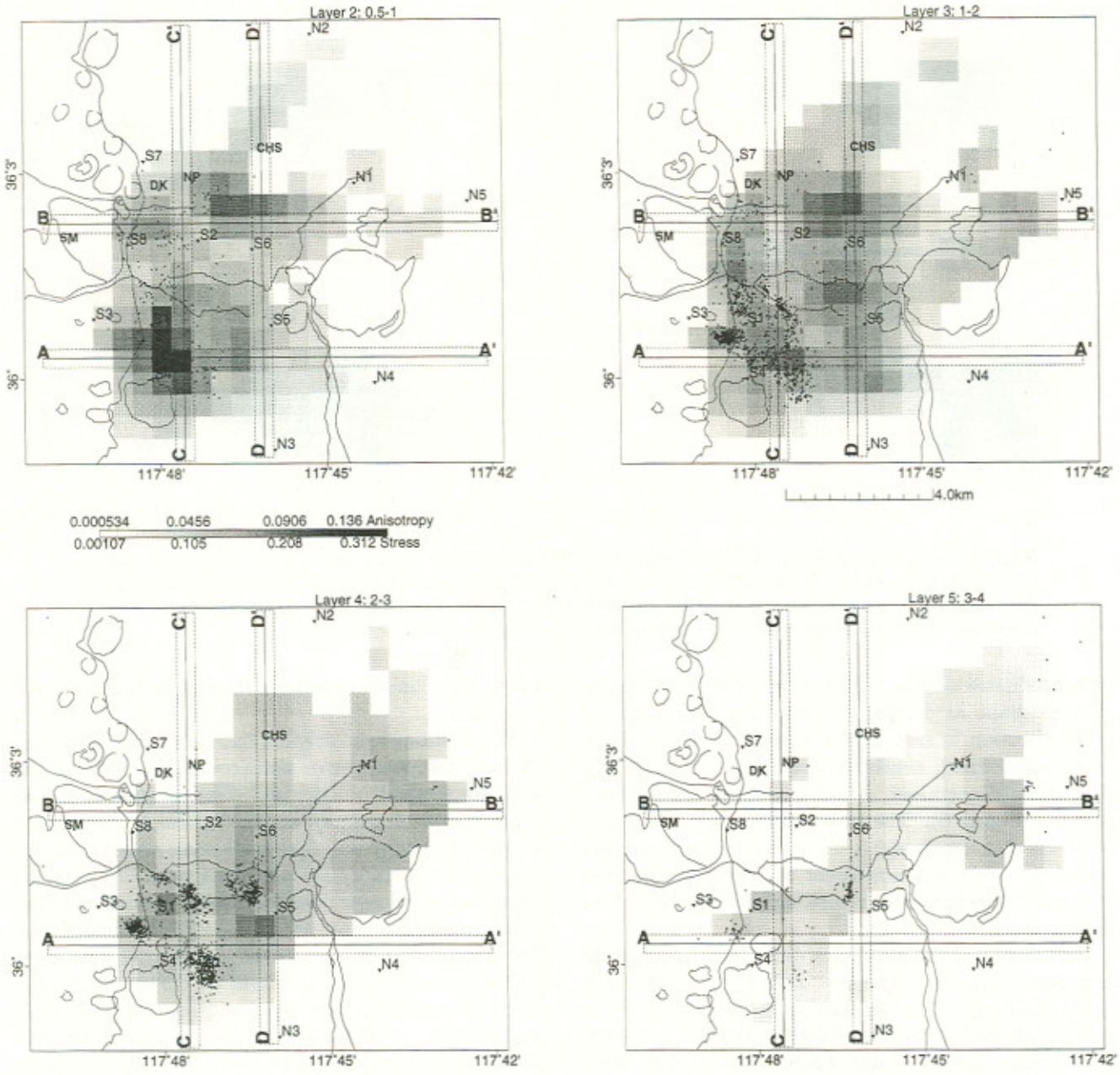

Figure 5. Distribution of anisotropic factor a_f. Dark shaded areas have large anisotropy. The largest anisotropy is found east of stations S1 and S4 at the relatively shallow depth of 0.5 – 1.0 km. The distribution of differential stress $(\alpha/K_0)(\sigma_1 - \sigma_2)$ is nearly linear with respect to a_f when a_f is small. Cross sections A through D are marked for reference.

and 8. The lengths of axis line segments are scaled by the product of the anisotropy factor a_f and projection cosines. Similar projections of the slow axes are provided in Figures 9 and 10. On the projections the fast axes may not be perpendicular to the slow axes. Fast directions of anisotropy are generally N-S trending at shallow depths and are oriented more easterly in the deeper parts of the model. Fast directions around station S6, however, are NE-SW at all depths. At depths 1–2 km between stations S5 and S6 there is an east-west trending, distinctive transition band of anisotropic directions, which corresponds to one arm of a circular, potentially porous and probably crack-rich zone [*Wu and Lees*, 1999b]. Anisotropic directions north and south of this transition band have approximately the same N-S trends. On cross section C-C' (Figure 8) the fast axes of this feature dip north, and the three-dimensional fast directions dip northeastward. Between S2 and S8, where the other arm of the circular velocity anomaly extends, no clear anisotropic transition appears to exist. If we trace the anisotropic transition band westward in depth, it appears to originate from below station S1 at a depth of 2–3 km, consistent with anomalies in V_p and V_s [*Wu and Lees*, 1999b] and V_p/V_s and $V_p * V_s$ (J. M. Lees and H. Wu, submitted to *J. Volc. Geotherm. Res.*, 1999). The distinctive anisotropic transition band may represent the trace of a fossil magmatic migration route. Anisotropic fast directions around S1–S4 are nearly uni-

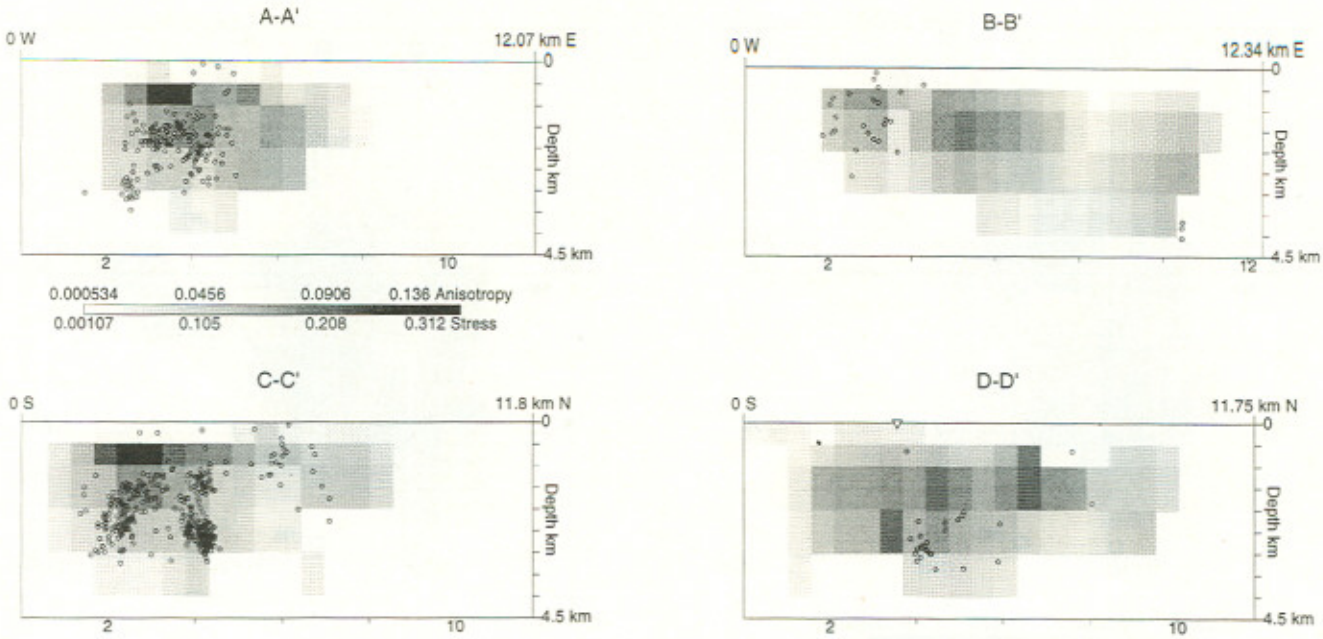

Figure 6. Cross sections of the anisotropic factor image (see Figure 5) for (left sections A and C and (right) sections B and D. Note the prominent, highly anisotropic feature below station S1. As in Figure 5, we present the scale for the differential stress direction. The largest concentration (dark shading) of differential stress is found around the S1-S3-S4 region.

form at shallow depths (< 2 km) and exhibit a roughly circular shape at depths > 2 km. No clearly defined gross direction is seen in the horizontal plane. However, well-defined, nearly vertical fast directions, dipping slightly northeast, are observed on vertical cross sections (Figure 8). The largest anisotropy, found east of S1–S4 at a depth of 0.5 – 1.0 km, has a nearly horizontal fast direction, consistent with spatial variations in stress derived from focal mechanisms [*Feng and Lees*, 1998].

Projections of the slow axes differ from those of the fast axes (Figure 9): The slow axes are predominantly E-W trending. The anisotropy transition band described above for the fast axes projections is evident for the slow axes in places where irregular slow directions are observed (Figure 9). Highly varying horizontal slow axes are observed around S1-S4, with nearly vertical slow axes seen on vertical cross sections (Figure 10). The vertical slow axes extend from the surface to a depth of ~3 km depth. On cross section C-C' a vertical anomalous swathe is bounded between two walls with differing anisotropy. The vertical swathe, 1.5 – 2.0 km wide, contains nearly vertical slow axes in contrast to the surrounding walls, which are more horizontally oriented, dipping south. The slow axis vertical swathe is part of the anisotropy transition band noted above.

6. Error Analysis

In this section, we discuss the error analysis as applied to the anisotropic inversion. The new method of anisotropic inversion presented by *Wu and Lees* [1999a] requires a new approach to estimating the errors of the anisotropic tomographic inversion. We present in appendix 1 a full description of our approach regarding this problem and here present the results applied to the Coso data.

We partitioned the original data set into 100 disjoint sets and computed error matrices ΔA_{ij} following the jackknife method of *Lees and Crosson* [1989]. Errors in anisotropic factor a_f appear randomly distributed (Figure 11), suggesting that systematic noise is not significant. Errors in a_f are ~1% over most of the target volume and are larger near the edge of good data distribution, where errors are as large as 2.5% in some blocks. Between S5 and S6, where an anisotropic transition band was found, errors are small (< 0.5%). In general, errors do not affect our main interpretations of gross anomalies in a_f (Figures 5 and 6). Errors in the fast directions (Figure 12) appear more spatially correlated (less random) than errors in a_f, and, on average, are ~6°. At shallow depths < 2 km, blocks southwest of S1 have larger errors than those northeast. The largest error in the entire target volume model is < 10°, suggesting that fluctuations in anisotropic directions associated with errors would not significantly alter our interpretations. Spatial resolution of the inversion is determined by examining point spread functions of a single-block anisotropy, checked in critical regions. These data are not presented here, because of limited space, but can be summarized: The horizontal resolution in the center of the model where ray coverage was adequate (estimated at ~1.5 blocks, i.e., ~1.0 km) and vertical resolution was ~1.5 km, i.e., 1.5 times layer thickness.

One of the most critical issues in anisotropic inversions is ray directional coverage, i.e., the distribution of directions sampled in each block. In anisotropic inversions, ray coverage has been shown to be more important than picking noise in arrival time estimation [*Wu*

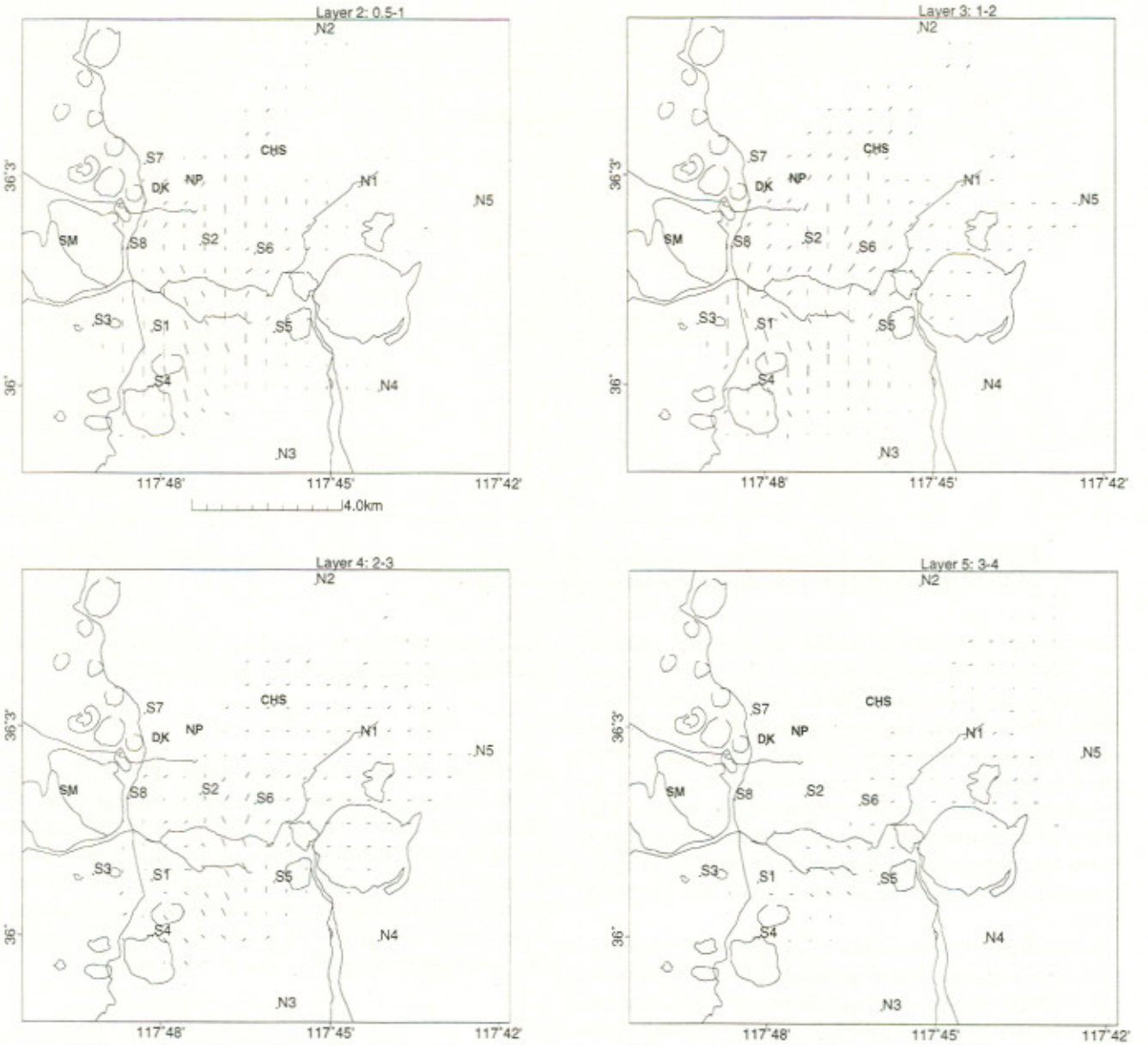

Figure 7. Plane view of fast directions. Projections of fast axes of velocity-squared ellipsoids scaled by anisotropic factors are plotted. The two blocks, whose ray coverages are shown in Figure 3, are plotted as shaded squares on layers 2 and 3, respectively.

and Lees, 1999a]. Deficiencies in ray coverage cannot be remedied via regularization techniques or smoothing and thus remain a permanent source of bias. We have explored the possibility of this bias contaminating our results by performing a synthetic inversion using the real ray distribution with a known anisotropy model. These results are presented in appendix 2.

7. Velocity Anisotropy, Stress, and Crack Distribution

Possible sources of seismic anisotropy in the crust include layering, crack alignment, deviatoric stress, and crystal preferred orientation [*Schön*, 1996]. Seismic reflection studies reveal that the Coso geothermal field is underlain by a relatively uniform granitic formation [*Malin*, 1994], and thus layering or rock composition are not likely to be major sources of anisotropy. On the other hand, cracks due to tectonic deformation and magmatic intrusions are pervasive in the Coso region; we assume they are the major sources of anisotropy. Deviatoric stress due to plate motion and regional shearing may be another contributor to anisotropy.

7.1. Stress-Induced Anisotropy

In this section, we consider the relationship of anisotropy and stress, with the intention of interpreting our anisotropy results primarily as a function of deviatoric stress. Later we will relax that assumption and consider other sources of anisotropy. The goal is to see how the three-dimensional variations of anisotropy shed light on otherwise unknown variations of physical parameters in the geothermal field.

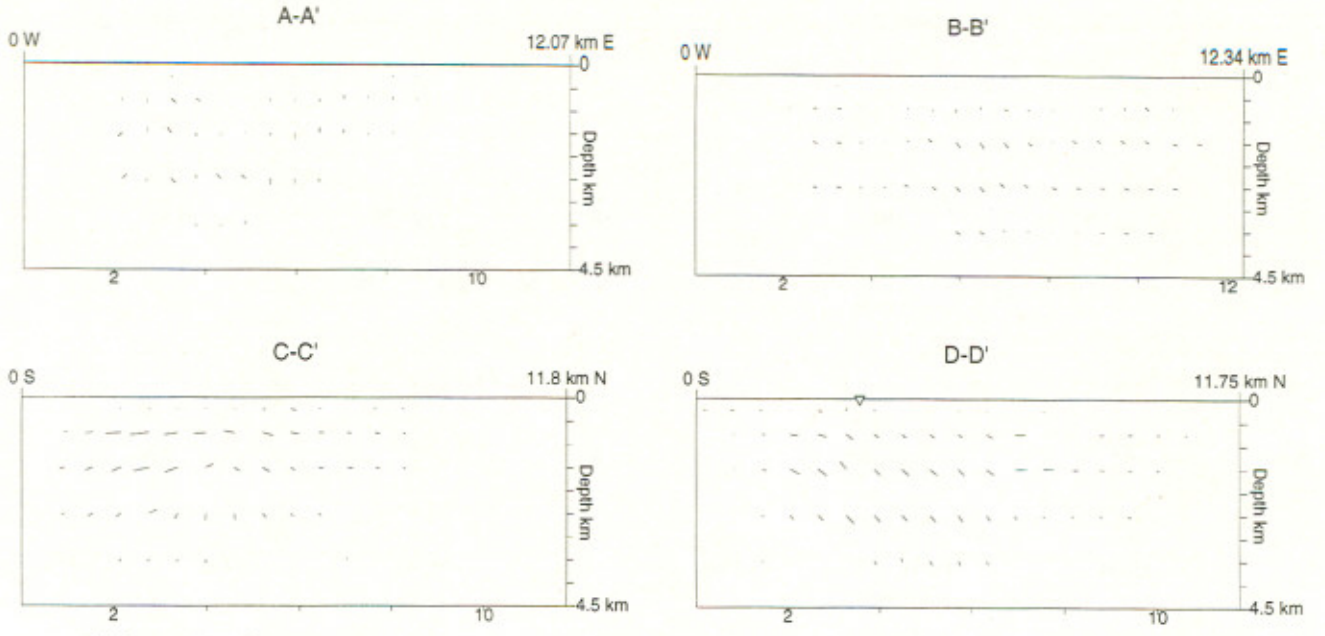

Figure 8. Cross sections of fast directions (see Figure 5). These are fast axes projected on four vertical cross sections. Fast directions are nearly vertical.

Deviatoric stress fields induce preferential opening and closing of cracks, potentially introducing seismic anisotropy in rocks [*Nur*, 1971; *Sayers*, 1988; *Schön*, 1996]. These effects are especially evident in cracked, porous media [*Gibson and Toksöz*, 1990]. Cracks oriented transverse to the compressional stress will be closed while stress parallel cracks remain open. This source of anisotropy provides a heuristic interpretation where fast velocities are parallel to cracks and slow velocities are perpendicular to cracks [*Nur and Simmons*, 1969].

Laboratory measurements of qP (quasi-P) wave velocities in a granite under uniaxial stress of 30 MPa report 13% anisotropy [*Nur and Simmons*, 1969], and fast velocities are observed parallel to compressional stress directions. Laboratory-observed anisotropy is thus substantial, considering that hydrostatic stress at 1 – 2 km depth is 30 – 60 MPa. If the subsurface lithology at Coso were known, we would be able to estimate, a priori, the differential stress distribution. Since this information is not available, we resort to a rough estimate of the stress field in the Coso region using our inversion results, assuming, at first, that anisotropy is primarily stress induced. Laboratory experiments show that for a porous medium the compressional stress-strain curve is concave up, i.e., $d^2\sigma/d\epsilon^2 > 0$. This fact, similar to "work hardening," is intuitive because a decrease in the number of open cracks increases the bulk modulus: Crack-free solids are generally harder to deform than cracked ones are. We also note that $dK/d\sigma > 0$, where $K = d\sigma/d\epsilon$ is the incremental bulk modulus. Since K determines the speed of compressional waves, we expect to observe faster velocities in high-stress directions (Figure 13).

Possible stress fluctuations in the shallow depths at Coso are probably small compared to whole Earth variations, and $dK/d\sigma$ in the stress range found at Coso can be approximated by a constant α such that

$$K \approx K_0 + \alpha\sigma \tag{6}$$

where constant K_0 is the extrapolated bulk modulus to the unstressed state. From experimental data on granite [*Nur and Simmons*, 1969] a rough estimate of $\alpha \approx 0.48 \times 10^3$, assuming rock density 2.7 g/cm^3. The magnitude of α is substantial, considering that the unstressed bulk modulus of the granite used in laboratory experiments was $K_0 = 45.4$ GPa (velocity 4.1 km/s) [*Nur and Simmons*, 1969]. The P wave velocity is

$$v = \sqrt{\frac{K}{\rho}} = \sqrt{\frac{K_0 + \alpha\sigma}{\rho}} \tag{7}$$

and the velocity anisotropy is thus

$$a_f = 2\frac{v_1 - v_2}{v_1 + v_2} = 2\frac{\sqrt{K_0 + \alpha\sigma_1} - \sqrt{K_0 + \alpha\sigma_2}}{\sqrt{K_0 + \alpha\sigma_1} + \sqrt{K_0 + \alpha\sigma_2}} \tag{8}$$

which does not depend on density explicitly. The differential stress can be written as

$$\frac{\alpha}{K_0}(\sigma_1 - \sigma_2) = \left(\frac{2 + a_f}{2 - a_f}\right)^2 - 1 = \frac{4a_f}{(2 - a_f)^2} \tag{9}$$

Equation (9) is general as long as (6) is valid. The distribution of the right-hand side, which is the differential stress scaled by α/K_0, is shown in Figures 5 and 6. For the Barre granite used by *Nur and Simmons* [1969], $K_0/\alpha = 94.6$ MPa. We use this figure at the Coso region because the Coso field is embedded in granitic bedrock. The average differential stress at Coso is ~2% of K_0/α, i.e., ~3 MPa (Figures 5 and 6). Since the bulk modulus K_0 increases with mean effective stress (depth), real dif-

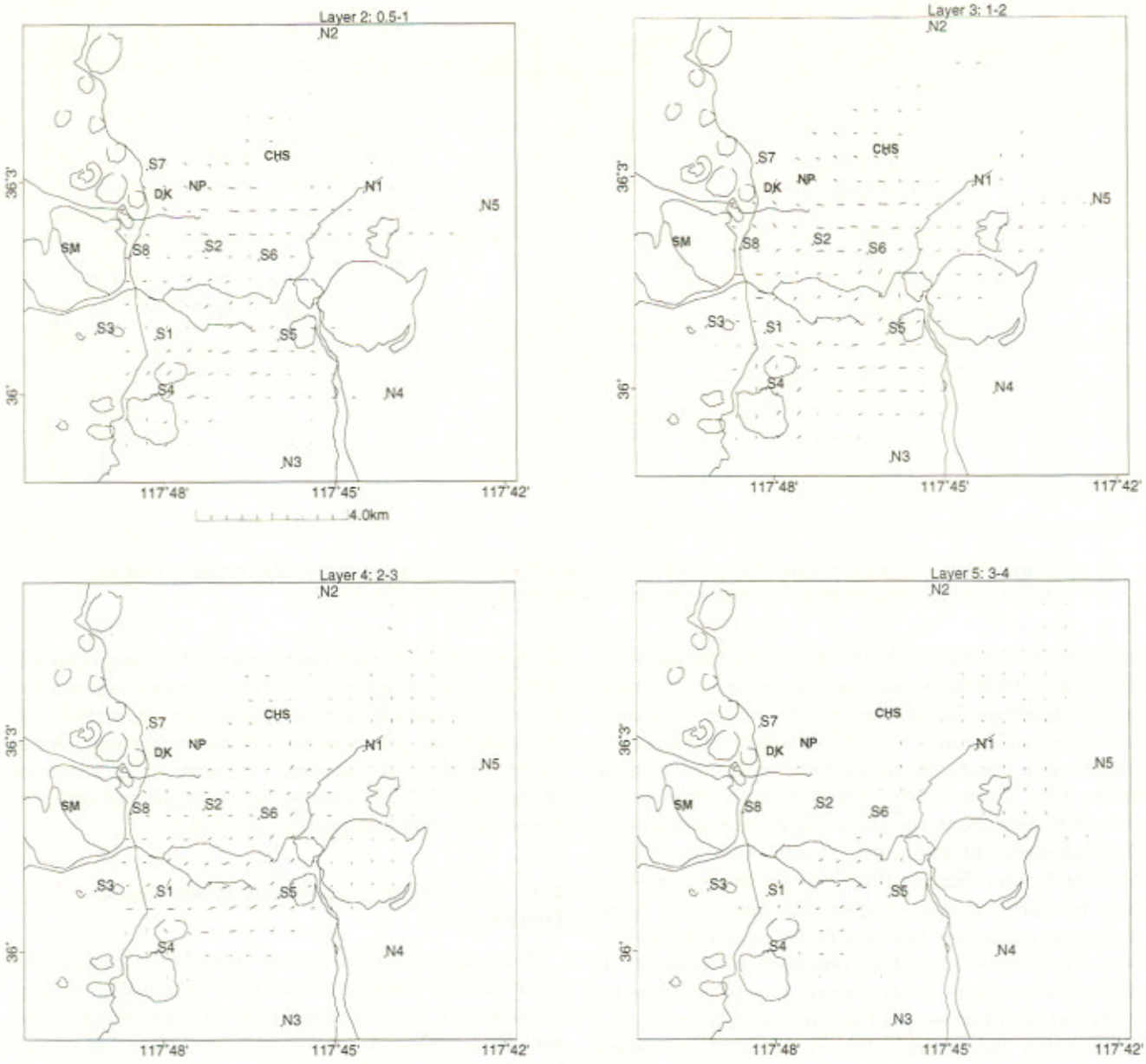

Figure 9. Plane view of slow directions. These are a_f-weighted projections of slow axes to horizontal plane. Note the E-W trending transition band between S5 and S6.

ferential stress may be larger than our estimates using ground-level measurements of K_0/α.

In general, large anisotropy indicates a large concentration of deviatoric stress and, consequently, associated seismicity. We note that there is a large concentration of deviatoric stress in the S1-S3-S4 region, where the largest number of earthquakes occurs (Figures 1 and 5). The deviatoric stress in S1-S3-S4 is ~4% of K_0/α, amounting to ~6 MPa, double the whole target average. Two other regions of stress concentration include one between S5 and S6, corresponding to a smaller cluster of events, and another between S6 and Coso Hot Springs, with no corresponding event cluster. Differential stress is largest at shallow depths (~1 km) and smaller in the deeper parts of the model (~3 km).

The stress directions derived here are consistent with regional tectonic shearing at Coso, with compressional axis NNE-SSW and dilational axis WNW-ESE in plane view [*Roquemore*, 1980]. Stress distribution based on focal mechanism inversion shows a significant change of stress in the S1-S3-S4 region [*Feng and Lees*, 1998], which is the area that also exhibits the largest deviatoric stress in our model (Figure 6).

7.2. Relationship of Stress and Crack Distribution

We next consider the possibility that stress alone is not the major contributor to anisotropy. Before we begin, though, we note that there is an intrinsic discrepancy between anisotropy directions induced by a stress field and anisotropy incurred by stress-induced shear cracks (fractures) (Figure 14). The fast directions produced by these two physical sources are 45° apart, and the true, overall anisotropic direction must

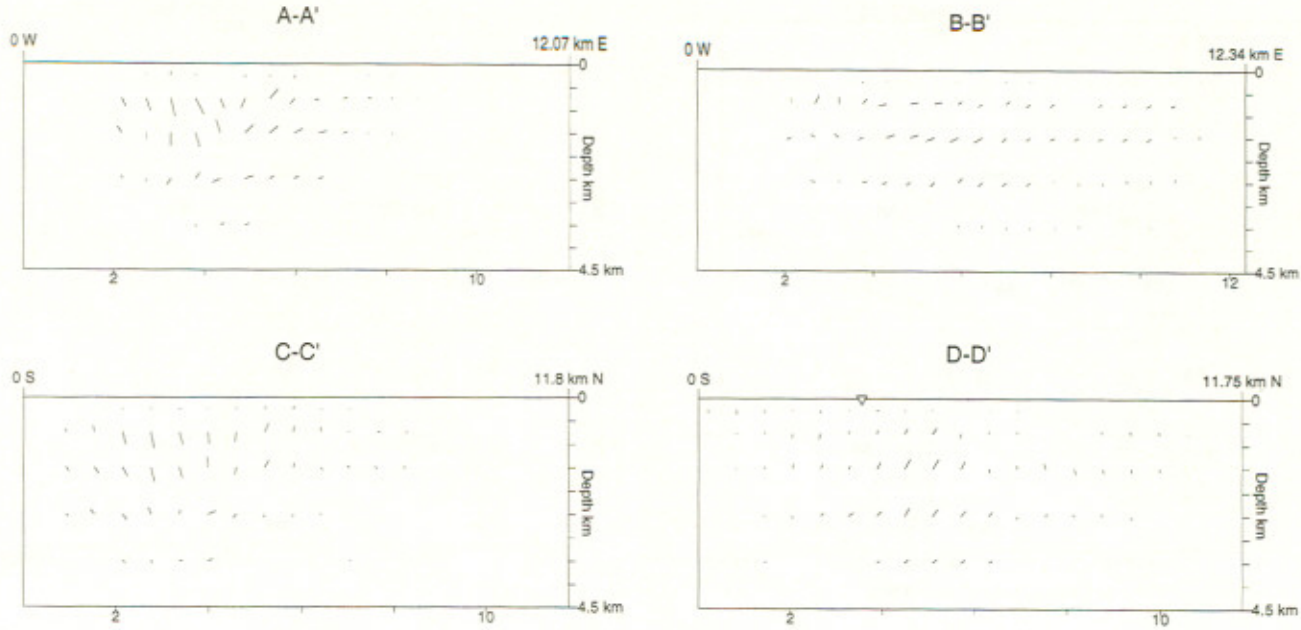

Figure 10. Cross sections of slow directions (see Figure 5). Note the vertically bounded feature in C-C' which has distinctive anisotropy compared with surrounding blocks.

be some combination of both. As an illustration of the directional differences, suppose we assume that cracks are the dominant factor, using an 80/20% ratio of crack and stress anisotropy. We will then have the situation presented in Figure 14, showing the vector orientations of the two effects. The overall fast direction is oriented 8.6° relative to the shear crack plane and 36.4° to the high-stress direction, using vector addition to combine the factors. Since stress fields are more short-lived than fractures, at least on geological timescales, cracks present in rocks may not be directly related to the current stress state but rather represent paleocracks. In this situation there is no obvious way to separate the contributions of stress and those of cracks on anisotropy. Considering the geologic history of the Coso region, however, a large number of cracks may be fossil and unrelated to the contemporary stress field. In this study, cracks and stress are assumed to be unrelated and have the same, additive anisotropic effects. The stress distribution in Figure 5 should thus be used cautiously when relating it to the current stress field. For example, the stress concentration noted in section 7.1 between Coso Hot Springs (CHS) and S6 may be an artifact associated with paleocracks. The stress state derived from focal mechanisms [*Feng and Lees*, 1998] represents the contemporary stress field and will differ, therefore, at least in part, from the stress distribution derived from anisotropy (Figure 5). If the fracture distribution can be determined by other, independent methods, such as S wave splitting or fluid flow observations, the stress state at Coso may be estimated more precisely from our inversion results.

Since we do not have a definitive way of distinguishing between these factors, we will treat them independently and interpret the results as if observed anisotropy is due solely to stress or crack distribution. This approach will surely be amended in the future as more information regarding crack orientation is collected. In section 7.3, we consider an interpretation of the anisotropy results based on crack distribution. We seek bulk properties of the rocks in the Coso geothermal field and compare them with other independent estimates.

7.3. Anisotropy Associated With Crack Distribution

When anisotropy is mainly induced by cracks, the crack density distribution may be obtained from perturbations of velocity associated with anisotropy [*Hudson*, 1981, 1994]. A cracked solid including flat, circular, aligned cracks behaves like a transversely isotropic body with P wave anisotropic factor a_f linearly related to crack density C_d [*Thomsen*, 1995]:

$$a_f = cC_d \tag{10}$$

where crack density C_d is the number of cracks per unit volume, $C_d = 3\phi/(4\pi a)$, ϕ is porosity, and a is the crack aspect ratio. The coefficient c depends on the bulk modulus K and Poisson's ratio σ of the uncracked solid, the bulk modulus K_f of the filling fluid (if any), and the aspect ratio a of the cracks [*Thomsen*, 1995; *Anderson*, 1989; *Babuska and Cara*, 1991]

$$c = \frac{32}{3}\left\{\frac{(1-\sigma)(1-\frac{K_f}{K})}{1-\frac{K_f}{K}+\frac{4}{3\pi a}\frac{K_f}{K}\frac{1-\sigma^2}{1-2\sigma}} - \frac{1-2\sigma}{2-\sigma}\right\} \tag{11}$$

For the crust we approximate $\sigma \approx 1/4$ and (11) can be simplified

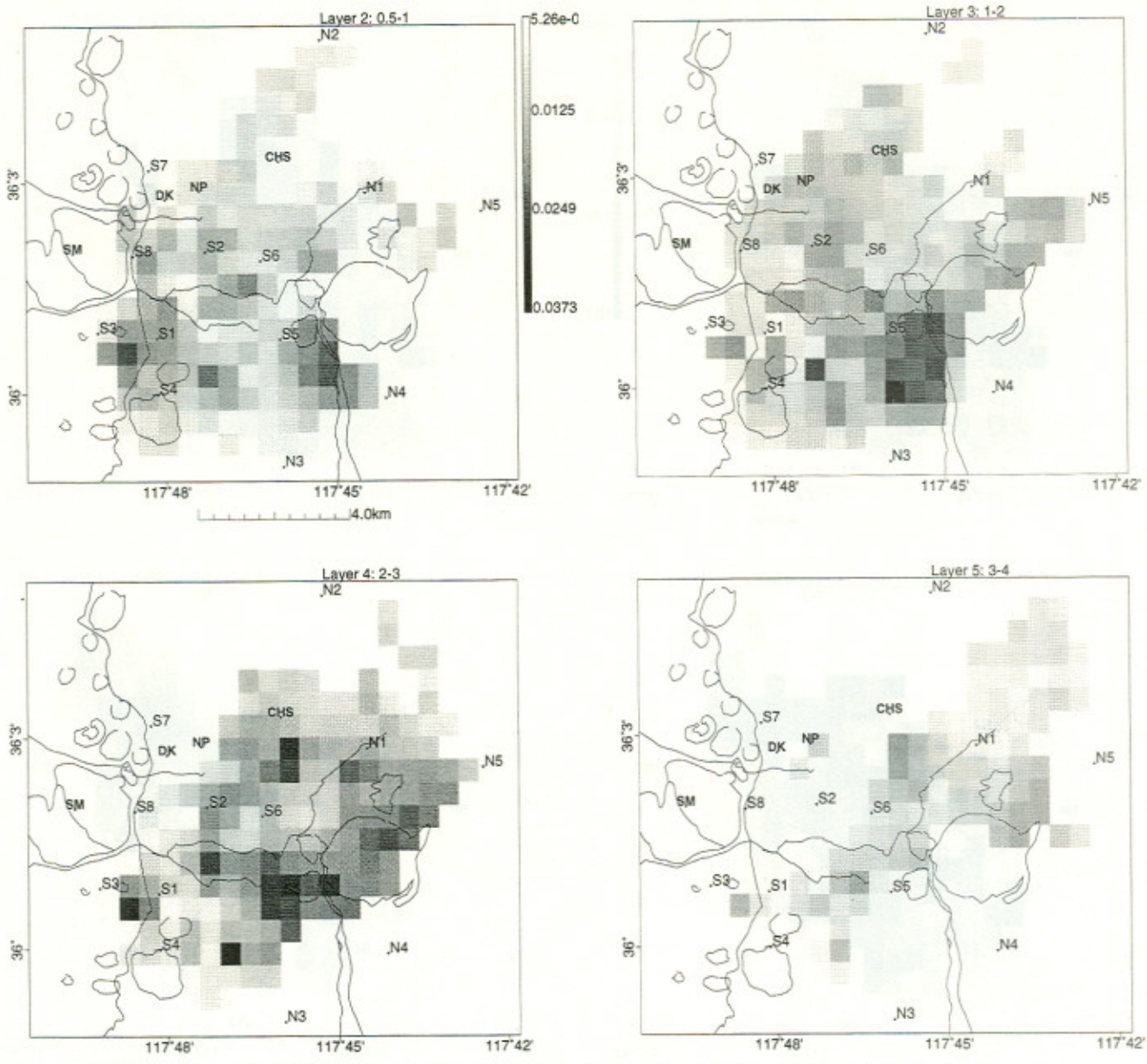

Figure 11. Jackknife errors in anisotropic factors a_f. In general, errors are ~1% and may be as large as 2.5% in some areas around the edge of the model.

$$c \approx 8\left\{\frac{1-\frac{K_f}{K}}{1-\frac{K_f}{K}(1-\frac{5}{2\pi a})}-\frac{8}{21}\right\} \tag{12}$$

For water-filled cracks in granite, $K_f/K \approx 0.020$[*Carmichael*, 1989] *and*

$$c = 8\left\{\frac{1}{1+\frac{1}{61.6a}}-0.381\right\} \tag{13}$$

Note that if a is sufficiently small (< 0.01), c could be negative, an intuitively incorrect result illustrating a limitation of the above assumption. As long as the aspect ratio of cracks is $\gg 1/60$, that factor may be dropped from (13) and $c = 104/21 = 4.95$. With a constant c the distribution of microcrack density C_d is just a scaled version of the anisotropic factor a_f by $1/c$ (Figure 5). Using an average anisotropic factor ~3.88%, the average crack density at Coso is $\bar{C}_d = 0.0078$, close to, though smaller than, $C_d = 0.010$~0.035 derived in the shear wave splitting analysis of *Luo and Rial* [1997]. The mismatch indicates that the aspect ratio of cracks at Coso may be close to 1/60. Taking an aspect ratio 1/60, we have $c = 0.952$, and the average crack density $\bar{C}_d = 0.041$, which is larger than previous shear wave splitting estimates. The best fit aspect ratio, a^*, for the median crack density given by the shear wave splitting study is $a^* = 1/38$.

In the above derivation we have made, perhaps, an unrealistic, theoretical assumption that all cracks are aligned. In a cracked solid where cracks are randomly oriented, no anisotropy should be expected. Anisotropy observed in the velocity is actually from the residual, unbalanced crack orientation distribution. The total

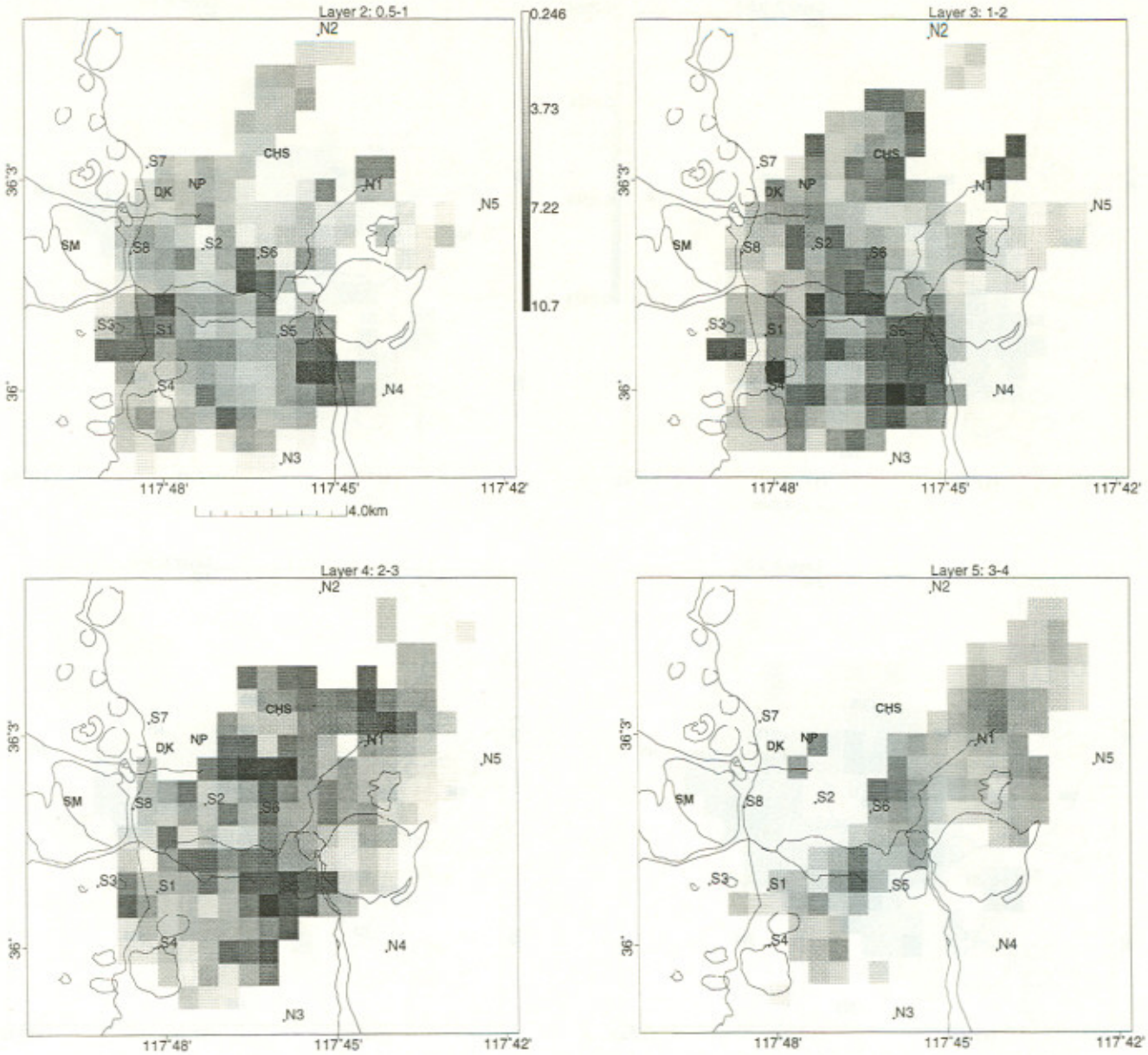

Figure 12. Jackknife errors in fast directions. Shown in Figure 12 are angles in degrees of deviation from fast directions. The largest error in the direction of the anisotropy is 10°.

crack density, i.e., the sum of randomly oriented and aligned crack densities, can be much larger if the isotropic part of the crack orientation distribution is large. This may explain the order of magnitude discrepancy of crack densities found between this study and those reported by *Feng and Lees* [1998]. Our estimates and those of *Luo and Rial* [1997] are, in fact, estimates of residual, anisotropic crack density. Unfortunately, knowledge about the isotropic part of crack orientation distributions cannot be obtained from velocity anisotropy alone.

7.4. Permeability and Velocity Anisotropy

For geothermal developers and researchers studying crustal fluid flow, one of the most important physical parameters is the permeability of rocks and the facility with which fluids may pass through. Using crack density and stress distribution derived from seismic anisotropy, an estimate of permeability distribution may be obtained via a statistical approach developed originally for randomly oriented microcracks under stress [*Gibson and Toksöz*, 1990]. In that study, anisotropies of both velocity and permeability were related to the orientation distribution of cracks. Previous studies have shown that velocity anisotropy can be used to estimate permeability orientation distribution, and these compared favorably with laboratory measurements [*Gibson and Toksöz*, 1990]. Permeability distribution was predicted from crack distributions via a parallel flow model. The aperture of cracks is $L_0 a$, where L_0 is crack length and permeability, k_1, of a single crack is calculated through an analysis of the fluid flow of a single parallel plane-walled fracture [*Snow*, 1969]:

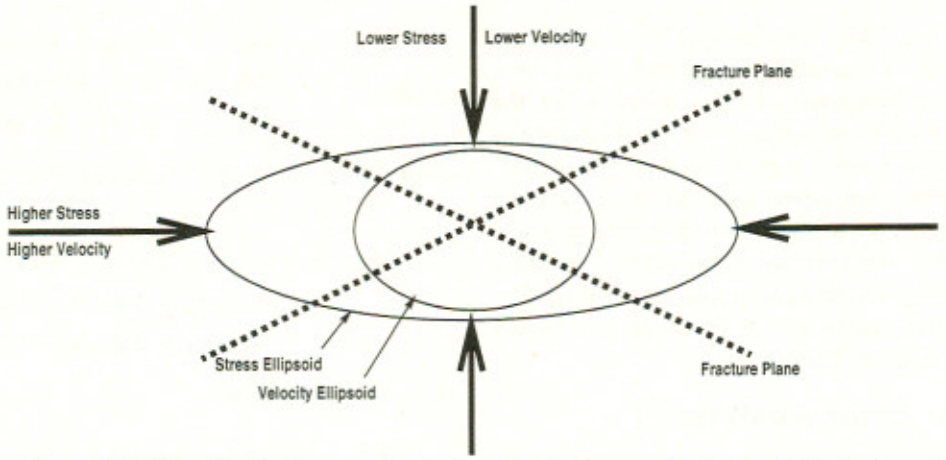

Figure 13. Relationship between principal axes of stress and those of the induced P wave velocity anisotropy. When stress-strain relation is concave, i.e., $d^2\sigma/d\epsilon^2 > 0$, high-stress direction corresponds with high P wave velocity.

$$k_1 = \frac{L_0^3 a^3}{12} \tag{14}$$

The total permeability k for aligned, identical cracks with density C_d would be

$$k = k_1 C_d = \frac{L_0^3 a^3}{12} C_d = \frac{L_0^3 a^3 a_f}{12c} \tag{15}$$

Equation (15) is obtained using (10). The distribution of permeability is thus proportional to the distribution of anisotropic factors for aligned, identical cracks. Comparison of the distribution of fluid flow and anisotropy thus may yield insights about the distribution of crack lengths, L_0, and crack aspect ratios a.

One caveat to the above discussion should be pointed out. We have assumed that crack density and its orientation fully determine preferred permeability directions. The isotropic crack orientation, however, determines the isotropic part of permeability orientation, and the residual crack orientation determines the anisotropic part of the permeability orientation. Only the residual crack orientation distribution, however, gives rise to velocity anisotropy. Since in this study we estimate the anisotropic crack distribution from velocity anisotropy, we can only determine the deviatoric, as opposed to the complete, permeability from our analysis. This may explain the order of magnitude discrepancy between theoretical predictions and laboratory measurements of permeability provided by *Gibson and Toksöz* [1990]. Velocity anisotropy and anisotropic permeability are related indirectly via crack orientation distribution. Unfortunately, an explicit, direct relationship between velocity anisotropy and permeability is as yet unknown. Qualitative analysis suggests that the fast velocity direction is probably the direction of the largest permeability and thus, intuitively, the probable fluid flow direction. While we do not have detailed knowledge of fluid flow or permeability distribution in the Coso geothermal field, we suggest here that seismic anisotropy provides a geophysical method to estimate flow patterns remotely. Our results can be tested, at least in principle, by drilling and sampling the regions we have imaged.

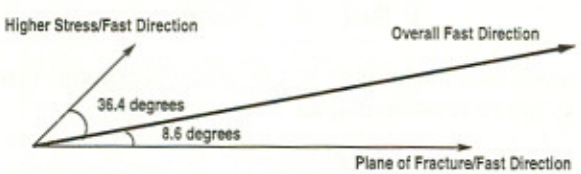

Figure 14. Superposition of stress-induced and crack-induced anisotropy when cracks are produced by the stress field. The ratio of the magnitudes of the anisotropy is arbitrarily chosen as 1:5; that is, 20% anisotropy is due to stress differential. The angle between the overall anisotropy direction and that of the cracks is 8.6°.

8. Conclusion

We have applied a new method for determining anisotropy tomography using a linear inversion of microseismic, P-wave traveltime data in the Coso geothermal field, California. The overall anisotropy at Coso is north-south fast in the western part and east-west fast in the eastern part of our target region. A large-amplitude (8%) anisotropy perturbation is found east of stations S1-S4. An irregular, E-W trending anisotropic transition band of width 1–2 km is identified between S5 and S6, and a circular structure is found around S1-S3-S4. Stress distribution and crack density are estimated from velocity anisotropy, and gross features of the distributions correlate well with other, independent studies using earthquake focal mechanisms. The distribution of deviatoric stress appears to correlate well with dense seismicity near S1-S3-S4 where the deviatoric stress is almost double the field average. This anomaly corre-

lates with high heat flow, attenuation anomalies, and a proposed model of upwelling magma [*Wu and Lees*, 1999b]. The estimated residual crack densities for the Coso region agree with a previous S wave splitting study [*Luo and Rial*, 1997] and range from 0.0078 to 0.041. The most probable crack aspect ratio at Coso, obtained through comparison with a previous S-splitting study, is ~1:38. Finally, the residual permeability distribution is estimated by assuming a simple planar fluid flow model through flat cracks and is found to be roughly proportional to velocity anisotropy.

Appendix A: Error Analysis

Model uncertainty and spatial resolution are determined by jackknife analysis and point spread functions of single anisotropic blocks in critical regions [*Lees and Crosson*, 1989], respectively. Jackknife error estimates produce an error matrix $\Delta A = \Delta e_{ij}$ whose elements are all positive. The following approach is used to estimate errors in the isotropic component, anisotropic factor a_f, and anisotropic principal directions due to small perturbations in A_{ij}. Errors in the isotropic component are simply the trace of the error matrix ΔA,

$$\epsilon_{\text{iso}} = \frac{1}{3}\sum_i \Delta A_{ii} \tag{A1}$$

and errors in the anisotropic factor a_f are computed through perturbations of the singular value decomposition (SVD) of A. Since A is symmetric positive definite (velocity $v = \mathbf{x}^T\mathbf{A}\mathbf{x}$), we have

$$A = a_1\mathbf{x}_1\mathbf{x}_1^T + a_2\mathbf{x}_2\mathbf{x}_2^T + a_3\mathbf{x}_3\mathbf{x}_3^T \tag{A2}$$

where $\mathbf{x}_i$ are the orthogonal eigenvectors of A and a_i are the positive singular values of A. Errors in the anisotropic factor a_f depend on errors in the singular values of A, a_i (equation (2)). Since $a_1 = \mathbf{x}_1\mathbf{x}_1^T : A_{ij}$ (double-dot product), errors in a_1 are approximated by

$$\epsilon(a_1) = \epsilon(A_{ij})\|x_{1i}x_{1j}\| \tag{A3}$$

Errors in a_2 and a_3 are computed similarly, and we obtain

$$\epsilon(a_1 - a_3) = \epsilon(A_{ij})(\|x_{1i}x_{1j}\| + \|x_{3i}x_{3j}\|) \tag{A4}$$

where $\epsilon(A_{ij}) = \|\Delta A\|$. Euclidean norms for matrices are used, i.e., $\|A\| = \sqrt{\sum_{ij} A_{ij}^2}$. When computing errors in the eigenvalues, the eigenvectors $\mathbf{x}_i$ are held constant, an approximation valid only for small perturbations ΔA. Errors in the anisotropic factor a_f are then obtained using (2).

By assuming small perturbations in A, errors in the eigenvectors may be estimated by holding the eigenvalues constant. Since small perturbations to unit vectors $\mathbf{x}_i$ are orthogonal to the unit vectors, i.e., $\Delta\mathbf{x}_i \perp \mathbf{x}_i$ when $|\Delta\mathbf{x}_i| << 1$, $\Delta\mathbf{x}_i$ may be linearly represented by the other two eigenvectors, such that

$$\begin{aligned}
\Delta\mathbf{x}_1 &= b_{12}\mathbf{x}_2 + b_{13}\mathbf{x}_3 \\
\Delta\mathbf{x}_2 &= b_{21}\mathbf{x}_1 + b_{23}\mathbf{x}_3 \\
\Delta\mathbf{x}_3 &= b_{31}\mathbf{x}_1 + b_{32}\mathbf{x}_2
\end{aligned} \tag{A5}$$

where b_{ij} are unknown constants. Perturbation of (A2) gives

$$\begin{aligned}
A+\Delta A = {} & a_1(\mathbf{x}_1 + \Delta\mathbf{x}_1)(\mathbf{x}_1^T + \Delta\mathbf{x_1}^T) \\
& + a_2(\mathbf{x}_2 + \Delta\mathbf{x}_2)(\mathbf{x}_2^T + \Delta\mathbf{x_2}^T) \\
& + a_3(\mathbf{x}_3 + \Delta\mathbf{x}_3)(\mathbf{x}_3^T + \Delta\mathbf{x_3}^T)
\end{aligned} \tag{A6}$$

and, after expansion,

$$\begin{aligned}
\Delta A = {} & a_1\mathbf{x}_1\Delta\mathbf{x}_1^T + a_2\mathbf{x}_2\Delta\mathbf{x}_2^T + a_3\mathbf{x}_3\Delta\mathbf{x}_3^T \\
& + a_1\Delta\mathbf{x}_1\mathbf{x}_1^T + a_2\Delta\mathbf{x}_2\mathbf{x}_2^T + a_3\Delta\mathbf{x}_3\mathbf{x}_3^T \\
& + a_1\Delta\mathbf{x}_1\Delta\mathbf{x}_1^T + a_2\Delta\mathbf{x}_2\Delta\mathbf{x}_2^T + a_3\Delta\mathbf{x}_3\Delta\mathbf{x}_3^T \\
= {} & \ldots + (a_2b_{21}^2 + a_3b_{31}^2)\mathbf{x}_1\mathbf{x}_1^T \\
& + (a_1b_{12}^2 + a_3b_{32}^2)\mathbf{x}_2\mathbf{x}_2^T \\
& + (a_1b_{13}^2 + a_2b_{23}^2)\mathbf{x}_3\mathbf{x}_3^T
\end{aligned} \tag{A7}$$

All terms are orthogonal to each other, and the omitted terms have the form $\mathbf{x}_i\mathbf{x}_j^T$ with $i \neq j$. We can find a rough error constraint on b_{ij} using the last three terms in (A7). To proceed, we decompose the error matrix ΔA on a complete set of bases $\mathbf{x}_i\mathbf{x}_j^T$, such that

$$\Delta A = c_{ij}\mathbf{x}_i\mathbf{x}_j^T \tag{A8}$$

where $c_{ij} = \Delta A : \mathbf{x}_i\mathbf{x}_j^T = \Delta A_{ij}x_ix_j$ (direct product). Comparison with (A7) yields

$$\begin{cases}
a_2b_{21}^2 + a_3b_{31}^2 &= c_{11} \\
a_1b_{12}^2 + a_3b_{32}^2 &= c_{22} \\
a_1b_{13}^2 + a_2b_{23}^2 &= c_{33}
\end{cases} \tag{A9}$$

Since $a_i > 0$, we obtain an estimate of the maximum values of b_{ij} as the following

$$\begin{cases}
|b_{12}| &\leq \sqrt{c_{22}/a_1} \\
|b_{13}| &\leq \sqrt{c_{33}/a_1} \\
|b_{21}| &\leq \sqrt{c_{11}/a_2} \\
|b_{23}| &\leq \sqrt{c_{33}/a_2} \\
|b_{31}| &\leq \sqrt{c_{11}/a_3} \\
|b_{32}| &\leq \sqrt{c_{22}/a_3}
\end{cases} \tag{A10}$$

or more succinctly, $|b_{ij}| \leq \sqrt{c_{jj}/a_i}$. Maximum errors in $\mathbf{x}_i$ are thus estimated as

$$\begin{aligned}
\Delta\mathbf{x}_1 &= \frac{1}{\sqrt{a_1}}(\sqrt{c_{22}}\mathbf{x}_2 + \sqrt{c_{33}}\mathbf{x}_3) \\
\Delta\mathbf{x}_2 &= \frac{1}{\sqrt{a_2}}(\sqrt{c_{11}}\mathbf{x}_1 + \sqrt{c_{33}}\mathbf{x}_3) \\
\Delta\mathbf{x}_3 &= \frac{1}{\sqrt{a_3}}(\sqrt{c_{11}}\mathbf{x}_1 + \sqrt{c_{22}}\mathbf{x}_2)
\end{aligned} \tag{A11}$$

where $c_{ii} \geq 0$ since the jackknife error matrix ΔA has all positive elements. We note that only the diagonal ele-

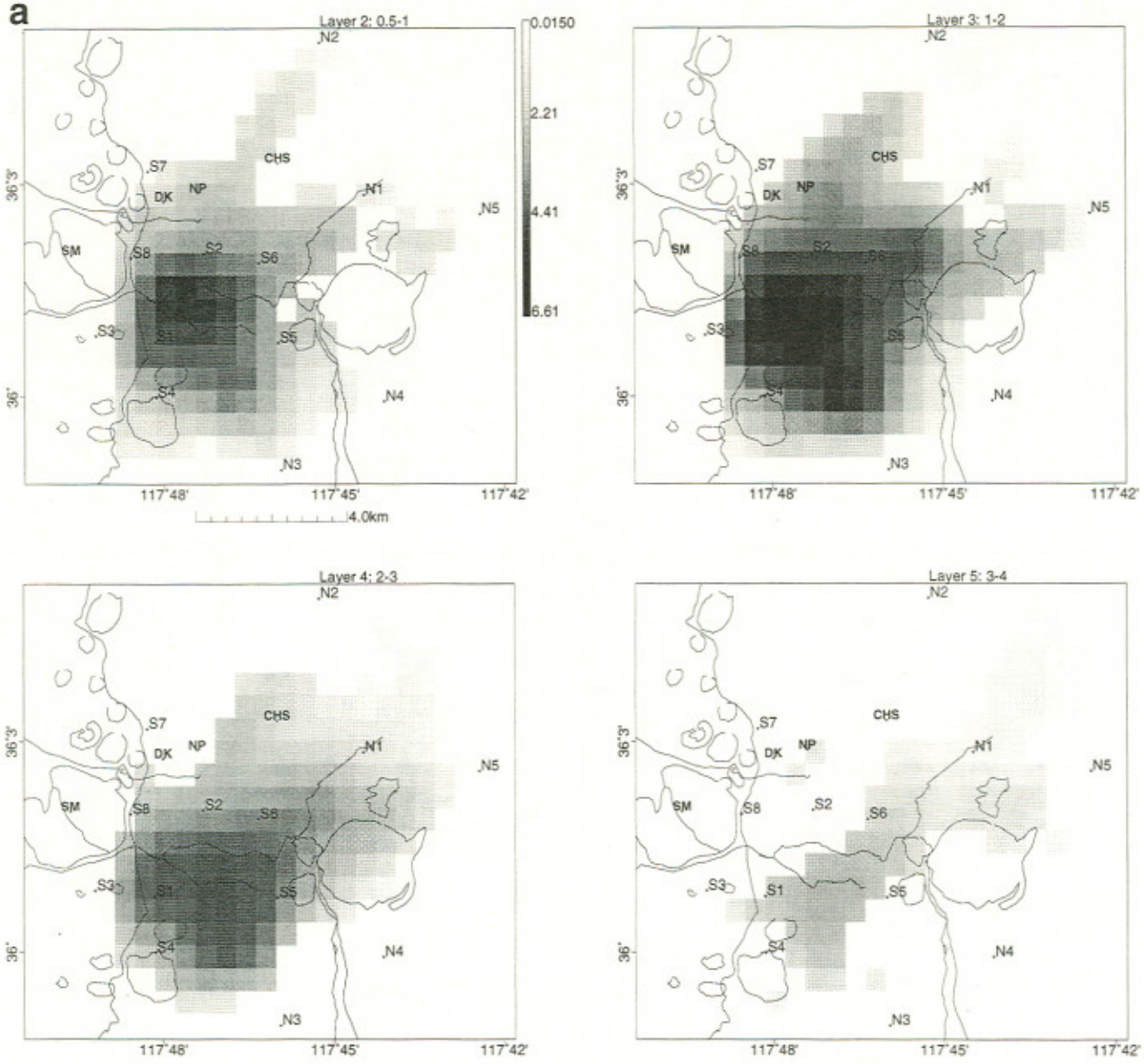

Figure 15. Recovered homogeneous anisotropy in an experimental inversion with the same rays as the real inversion. The original anisotropy is $a_f = 5\%$, and the effects of ray directional coverage are not prominent except around the edge of the model. The inversion parameters are exactly the same as those in the real inversion. (a) Recovered anisotropic factor a_f. (b) Recovered anisotropic direction. Shown in Figure 15b are projections of fast axes scaled by the recovered anisotropic factor. (c) Cross sections of Figure 15b (see Figure 5).

ments of ΔA contribute to error estimates of $\mathbf{x}_i$. There is some instability in the direction of anisotropy with respect to perturbations in A. For example, a small change in the shape of velocity ellipsoid, i.e., small ΔA, may result in up to 90° change in the fast direction. In the final results, anisotropy may appear to change significantly in adjacent blocks (Figures 7 and 9). While the matrix A is smoothed by regularization, the transformation of A to principal directions may not appear as smoothly varying. As a result, we look for general trends in the orientation and avoid interpretation of individual points in the model.

Appendix B: Synthetic Inversion

To investigate the extent of the influence of ray coverage used in this study, an experimental inversion was performed using a synthetic data set generated from a homogeneous e_{ij} model using the same ray coverage as that in the real data set. The homogeneous medium is transversely isotropic with fast symmetry axis inclined upward toward N45°E, where $A = v_0(I_{ij} + e_{ij})$ with

$$e_{ij} = \frac{1}{3}\begin{pmatrix} 0 & 0.05 & 0.05 \\ 0.05 & 0 & 0.05 \\ 0.05 & 0.05 & 0 \end{pmatrix} \qquad \text{(B1)}$$

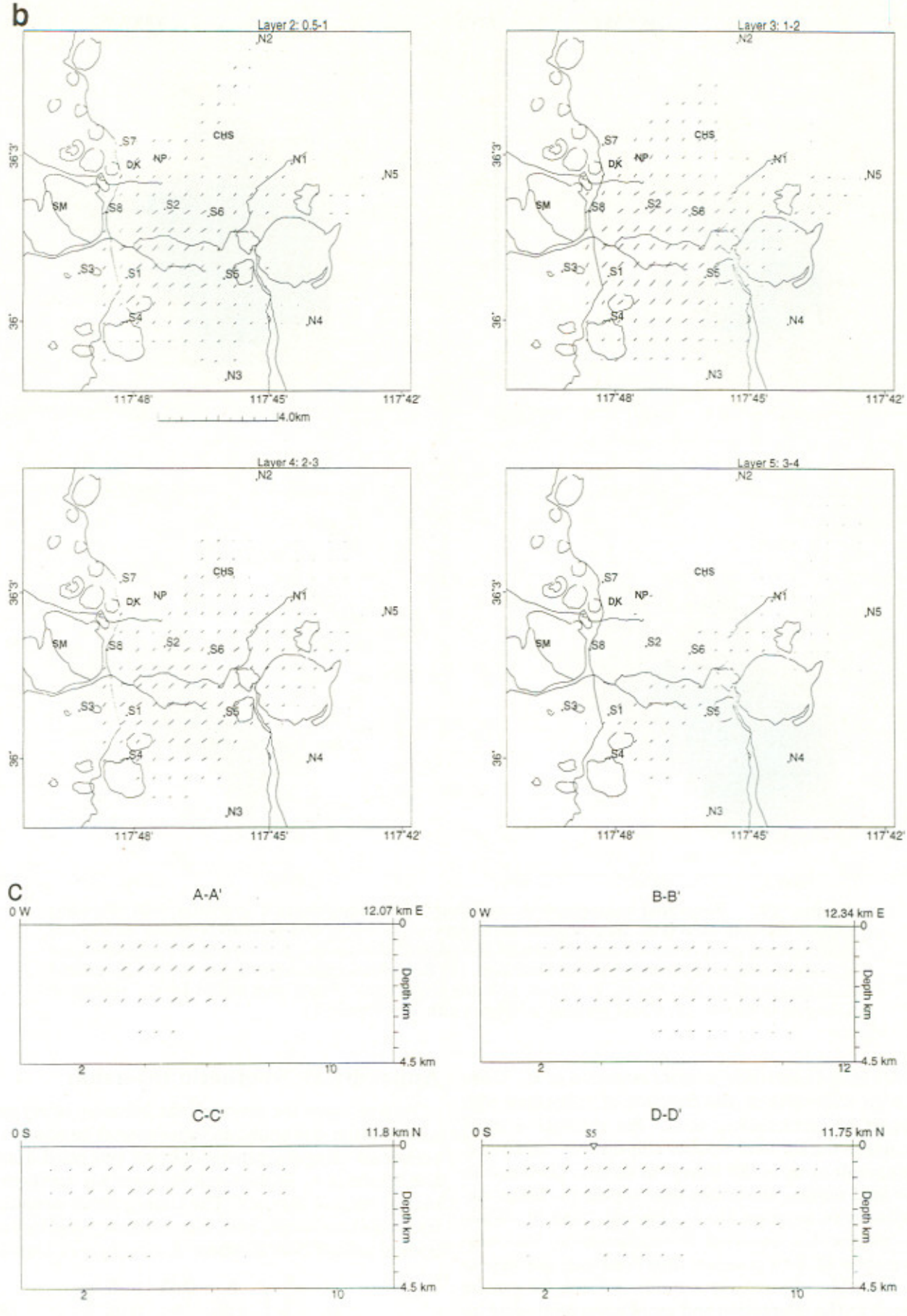

Figure 15. (continued)

where the magnitude of anisotropy is $a_f = 5\%$. The synthetic data were inverted using the same regularization parameters as those in the real data inversion, and variance reduction was 99%. Since the synthetic data were noise-free, the original, homogeneous model was correctly reconstructed (Figure 15). The anisotropic factor a_f was recovered best in the densely covered central region of the model (Figure 15a), particularly near stations S1-S4. The second regularization coefficient, λ_2, took control around the edge of the model where ray coverage was mostly unidirectional and, as a result, virtually eliminated anisotropies in these boundary blocks, indicating that the regularization was chosen appropriately. The experiment suggests that anisotropic directions, which may be more useful for constructing structural models than simple anisotropy perturbations, appear to be better resolved in the real inversion than a_f.

Acknowledgments. The authors thank the Navy Geothermal Program for funding this project (award N68936-94-R-0139) and providing data. We further acknowledge CalEnergy Co. Inc. and Peter Malin (Duke University) for data and valuable comments.

References

Anderson, D. L., *Theory of the Earth*, 366p, Blackwell Sci., Cambridge, Mass., 1989.

Babuska, V., and M. Cara, *Seismic Anisotropy in the Earth*, Kluwer Acad., Norwell, Mass., 1991.

Carmichael, R.S., *Practical Handbook of Physical Properties of Rocks and Minerals*, CRC Press, Boca Raton, Fl., 1989.

Combs, J., and Y. Rostein, Microearthquake studies at the Coso geothermal area, China Lake, California, in *Proceedings of the 2nd United Nations Symposium on the Development and Use of Geothermal Resources*, vol. *2*, pp. 909-916, U. S. Government Printing Office, Washington, D.C., 1976.

Crampin, S., Effective anisotropic elastic constants for wave propagation through cracked solids, in *Proceedings of the First International Workshop on Seismic Anisotropy* vol. 76, no. 1, edited by S. Crampin, R. G. Hipkin, and E. M. Chesnokov, pp. 135-145, Blackwell, London, 1984.

Duffield, W. A., and C. R. Bacon, Geologic map of the Coso volcanic field and adjacent areas, Inyo County, California, *U.S. Geol. Surv. Misc. Invest. Ser., MAP-1200*, 1981.

Feng, Q., and J. M. Lees, Microseismicity, Stress, and fracture within the Coso geothermal field, California, *Tectonophysics*, *289*, 221-238, 1998.

Gibson, R.L., and M.N. Toksöz, Permeability estimation from velocity anisotropy in fractured rock, *J. Geophys. Res.*, *95*, 15,643-15,655, 1990.

Hirahara, K., Detection of three dimensional velocity anisotropy, *Phys. Earth Planet. Inter.*, *51*, 71-85, 1988.

Hudson, J. A., Wave speeds and attenuation of elastic waves in material containing cracks, *Geophys. J. R. Astron. Soc.*, *64*, 133-150, 1981.

Hudson, J. A., Overall properties of anisotropic materials containing cracks, *Geophys. J. Int.*, *116*, 279-282, 1994.

Leary, P. C., and T. L. Henyey, Anisotropy and fracture zones about a geothermal well from *P*-wave velocity profiles, *Geophysics*, *50*, 25-36, 1985.

Lees, J. M., and R. S. Crosson, Tomographic inversion for three dimensional velocity structure at Mount St. Helens using earthquake data, *J. Geophys. Res.*, *94*, 5716-5728, 1989.

Luo, M., and J. A. Rial, Characterization of geothermal reservoir crack patterns using shear-wave splitting, *Geophysics*, *62*, 487-494, 1997.

Malin, P., The seismology of extensional hydrothermal system, *Trans. Geotherm. Resour. Counc.*, *18*, 17-22, 1994.

Nur, A., Effects of stress on velocity anisotropy in rocks with cracks, *J. Geophys. Res.*, *76*, 2022-2034, 1971.

Nur, A., and G. Simmons, Stress-induced velocity anisotropy in rock: An experimental study, *J. Geophys. Res.*, *74*, 6667-6674, 1969.

Pratt, R. G., W. J. McGaughey, and C. H. Chapman, Anisotropic velocity tomography: A case study in a near surface rock mass, *Geophysics*, *58*, 1748-1763, 1993.

Roquemore, G., Structure, tectonics, and stress of the Coso Range, Inyo County, California, *J. Geophys. Res.*, *85*, 2434-2440, 1980.

Sayers, C.M., Stress-induced ultrasonic wave velocity anisotropy in fractured rock, *Ultrasonics*, *26*, 311-317, 1988.

Schön, J.H., *Physical Properties of Rocks: Fundamentals and Principles of Petrophysics: Hand. of Geophys. Explor.*, vol. 18, edited by K. Helbig and S. Treitel, Pergamon, Tarrytown, N. Y., 1996.

Shalev, E., and M. Luo, A preliminary tomographic inversion of crack density in the Coso geothermal field (abstract), *Eos Trans. AGU*, *76*(46), Fall Meet. Suppl., F351, 1995.

Snow, D.T., Anisotropic permeability of fractured media, *Water Resour. Res.*, *5*, 1273-1289, 1969.

Thomsen, L.A., Elastic anisotropy due to aligned cracks in porous rock *Geophys. Prospect.*, *43*, 805-829, 1995.

Walck, M. C., Three-dimensional V_p/V_s variations for the Coso region, California, *J. Geophys. Res.*, *93*, 2047-2052, 1988.

Walck, M. C., and R. W. Clayton, *P* wave velocity variations in the Coso region, California, derived from local earthquake travel times, *J. Geophys. Res.*, *92*, 393-405, 1987.

Wu, H., and J. M. Lees, Attenuation structure of Coso geothermal area, California, from *P* wave pulse widths, *Bull. Seismo. Soc. Am.*, *86*, 1574-1590, 1996.

Wu, H., and J. M. Lees, Cartesian parameterization of anisotropic traveltime tomography, *Geophys. J. Int.*, *137*, 64-80, 1999a.

Wu, H., and J. M. Lees, Three-dimensional *P* and *S* wave velocity structures of Coso geothermal area, California, from microseismic traveltime data, *J. Geophys. Res.*, *104*, 13,217-13,233, 1999b.

Young, C. Y., and R. W. Ward, Three-dimensional Q^{-1} model of the Coso Hot Springs known geothermal resource area, *J. Geophys. Res.*, *85*, 2459-2470, 1980.

J. M. Lees and H. Wu, Department of Geology and Geophysics, Yale University, New Haven, CT 06510. (lees@love.geology.yale.edu)

(Received May 6, 1998; revised April 16, 1999; accepted April 27, 1999.)